Materials Advances

Accepted Manuscript

This article can be cited before page numbers have been issued, to do this please use: S. Jamshaid, H. Miyazaki, K. Kimura, K. Hayashi and P. Wellmann, *Mater. Adv.*, 2026, DOI: 10.1039/D6MA00113K.

ROYAL SOCIETY OF CHEMISTRY

rsc.li/materials-advances

Electronic Structure and Band Gap Modulation of Ba–S Compounds via Tuned Hybrid Functional Calculations

Sumbal Jamshaid[1,2], Hidetoshi Miyazaki[2], Koji Kimura[2], Koichi Hayashi[2], Peter Wellmann[1]
[1]Crystal Growth Lab, Materials Department 6, University of Erlangen-Nürnberg, 91058 Erlangen, Germany,
[2]Department of Physical Science and Engineering, Nagoya Institute of Technology, Gokiso, Showa, Nagoya 466-8555, Japan
*sumbal.jamshaid@fau.de

Keywords: Ba-S compounds, Hybrid functional, Band gap, Structural symmetry, Electron localization

This work presents a combined theoretical and experimental investigation of optimized crystal structural and electronic properties of Ba-S compounds (BaS, BaS_2, BaS_3). Films were synthesized via e-beam evaporation followed by sulfurization, yielding phase pure Ba-S compounds as confirmed by XRD. Optical measurements revealed a systematic reduction in band gap from BaS (≈3.8 eV) to BaS_2 (≈2.9 eV) and BaS_3 (≈2.6 eV), consistent with increasing sulfur coordination and the formation of S–S bonds. To interpret these results, DFT calculations were performed using the HSE06 hybrid functional, with systematic tuning of the HFSCREEN parameter to improve agreement with experiment. The results reveal a progressive narrowing of the band gap across the Ba–S series, following the trend BaS (≈3.8 eV) > BaS_2 (≈2.7 eV) > BaS_3-tetragonal (≈2.7 eV). This reduction is attributed to enhanced S–S bonding, polysulfide chain formation, and increased contributions from S 3p orbitals, which introduce new states near the Fermi level. The HFSCREEN (μ) parameter was systematically varied and selected to reproduce the experimental band gaps while maintaining consistency with expected screening trends across the Ba–S series. Overall, HFSCREEN-enhanced hybrid functional calculations provided more accurate band gap predictions than the GGA/PBE method, successfully capturing observed trends and reflecting key structure–property relationships within the Ba–S compounds.

Introduction:

Barium monosulfide (BaS) is considered a binary semiconductor of the Group 2 elements (alkaline earth metals) and the Group 6 elements (chalcogens), also known as a Group II-VI semiconductor. Barium sulfide compounds serve as crucial intermediate phases in the synthesis of chalcogenide perovskites such as $BaZrS_3$, which are widely investigated for optoelectronic applications with band gaps in the range of 1.7–2.1 eV [1–6]. Among Ba-S compounds, BaS_3 is particularly suitable for synthesizing Chalcogenide perovskites due to its relatively low melting point of 554 °C, compared with BaS (1200 °C) and BaS_2 (925 °C) [2,7–12]. The synthesis of alkaline earth (AE) metal polysulfides is highly dependent on reaction temperature, following a trend where higher temperature yield shorter polysulfide chain lengths (lower n values), and lower temperatures allow access to longer chain lengths[7]. Despite this relevance, Ba–S compounds remain relatively less explored—particularly their structural and electronic properties—which are critical for identifying and managing Ba–S secondary phases that can form in $BaZrS_3$ layers.

In this context, Ba–S compounds offer a tunable electronic platform governed by sulfur coordination chemistry. As the sulfur content increases from BaS to BaS_2 and BaS_3, the local

View Article Online
DOI: 10.1039/D6MA00113K

sulfur environment evolves from isolated S^{2-} anions to S_2^{2-} dimers and extended S_3^{2-} polysulfide chains. Similar sulfur-driven band-edge shifts and optical gap evolution have been reported in oxide-to-sulfide systems, where O→S substitution introduces higher-energy chalcogen p states and reduces the band gap [13]. This systematic change in sulfur coordination introduces S–S bonding, reduces crystal symmetry, and enhances the contribution of S 3p orbitals near the valence-band edge, enabling predictable band-gap modulation across the Ba–S series. Such coordination-dependent electronic screening effects have also been systematically analyzed in first-principles studies of sulfur substitution in perovskite-derived oxides [14].

Similar coordination-driven electronic trends are well established in the selenium analogs $BaSe_2$ and $BaSe_3$, which are nonmetallic polyselenides formally described as $Ba^{2+}(Se_2)^{2-}$ and $Ba^{2+}(Se_3)^{2-}$. These compounds host Se–Se units that enhance Se 4p–4p interactions and shift the band gap to lower energies, resulting in optical band gaps near ~2 eV, slightly larger for $BaSe_2$ than for $BaSe_3$. In contrast, sulfur-based analogs remain far less investigated, despite their relevance to sulfide-based optoelectronic materials [15].

The accurate computational estimation of the band gaps is essential for modeling and designing semiconductors used in photovoltaics, light-emitting diodes, and photoelectrochemical cells. Chalcogens can also form polychalcogenide chains of different lengths (Xn^{2-}, $n \geq 2$), which display unique chemical behavior and enable access to kinetically stabilized or metastable materials with unusual chemical and physical properties [16]. Polysulfides are especially important in metal–sulfur batteries, most notably in Li–S systems [17]. However, quantitatively capturing the electronic structure of such sulfur-rich systems remains a significant theoretical challenge.

Of the numerous computational techniques, density functional theory (DFT) is the most used for extended solid state systems as it offers a good compromise between accuracy and computational cost. Yet, an accurate estimate of the energy band gap (E_g) is still an unresolved issue [18]. Many of such atomic-scale techniques have been tried, with DFT being the most popular one, in which the calculated E_g) is heavily influenced by the selection of exchange–correlation functional [19]. However, standard local and semilocal density functional approximations—such as the Local Density Approximation (LDA) and Generalized Gradient Approximation (GGA) typically suffer from a significant underestimation of band gaps. One of the commonly used GGA functionals is the Perdew–Burke–Ernzerhof (PBE) functional [20]. This shortcoming arises from self-interaction errors and the absence of the derivative discontinuity in the exchange–correlation potential, which are inherent limitations of these functionals [21].

To address this issue, hybrid functionals that incorporate a portion of nonlocal Hartree–Fock (HF) exchange have been developed. These hybrid approaches, such as the HSE06 functional, can significantly improve band gap predictions by mitigating self-interaction errors. However, this improved accuracy comes at the cost of increased computational demand, making hybrid functionals more expensive than semilocal ones [22].

While hybrid functionals such as HSE06 significantly improve band gap predictions compared to semilocal DFT, they do not represent a true quasiparticle approach (e.g., GW) and do not explicitly include excitonic effects. Therefore, comparisons between calculated and experimentally measured optical band gaps should be interpreted with these limitations in mind.

View Article Online
DOI: 10.1039/D6MA00113K

In this work, we present a combined experimental and theoretical investigation of Ba–S thin films aimed at elucidating the structure–property relationships governing electronic band-gap evolution across the Ba–S series. Ba–S compounds were synthesized using a thin-film stacked-layer approach followed by controlled sulfurization, a strategy well established for other chalcogenide semiconductors such as kesterites and chalcopyrites. The effects of synthesis temperature on phase formation were systematically examined, and the single-phase nature of the resulting films was confirmed by X-ray diffraction. Optical measurements were used to characterize the band-gap evolution from BaS to sulfur-rich phases. Complementary first-principles calculations were performed using hybrid density functional theory, in which the exact-exchange mixing parameter was fixed while the range-separation parameter (HFSCREEN) was systematically varied to explore how crystal symmetry and local bonding motifs influence electronic screening and band-gap formation. By directly correlating experimental optical data with hybrid-functional electronic structure calculations, this integrated approach provides a consistent framework for understanding sulfur-coordination-driven bandgap tuning and offers predictive insight into the formation and control of Ba–S secondary phases in chalcogenide perovskites and related sulfide semiconductors.

Experimental & Computational Section

Thin Film Fabrication:

BaS, BaS_2, and BaS_3 thin films were fabricated on 12 × 12 mm glass substrates using a two-step sequential process. In the first step, barium monosulfide (BaS, Alfa Aesar, 99.9%) was deposited via electron beam (e-beam) evaporation using an Edwards E306A deposition system. All substrates were thoroughly cleaned prior to deposition in an ultrasonic bath using a 1:1 mixture of acetone and isopropanol for 10–15 minutes to remove organic and particulate surface contaminants.

BaS thin films were deposited to a thickness ranging from 300-350 nm, Film thickness was monitored using a quartz crystal microbalance (FTM5, Edwards), The estimated uncertainty in thickness is ~5%. The deposition rate was carefully maintained between 0.1–0.2 nm/s for BaS to ensure uniform coverage. As-deposited BaS films appeared transparent with a light bluish pink hue.

Sulfurization Process:

In the second step, selected BaS films were sulfurized in a quartz tube furnace to form BaS_2 and BaS_3 phases shown in Figure 1 (a). The films were placed in a graphite box along with 80-90 mg of elemental sulfur (Alfa Aesar, 99.5%, sublimed, 100 mesh) and inserted into the hot zone of the preheated furnace. Sulfurization was carried out under a constant nitrogen flow to maintain an inert atmosphere, using 100 sccm for BaS_2 and 50 sccm for BaS_3 synthesis. The annealing temperatures ranged from 300 to 350 °C were carefully controlled using an optical pyrometer. Sulfurization durations were fixed at 30 minutes for all samples. The synthesis conditions were optimized for phase purity; annealing at approximately 300 °C yielded BaS_3, while increasing the temperature to ~350 °C resulted in the formation of BaS_2.

View Article Online
DOI: 10.1039/D6MA00113K

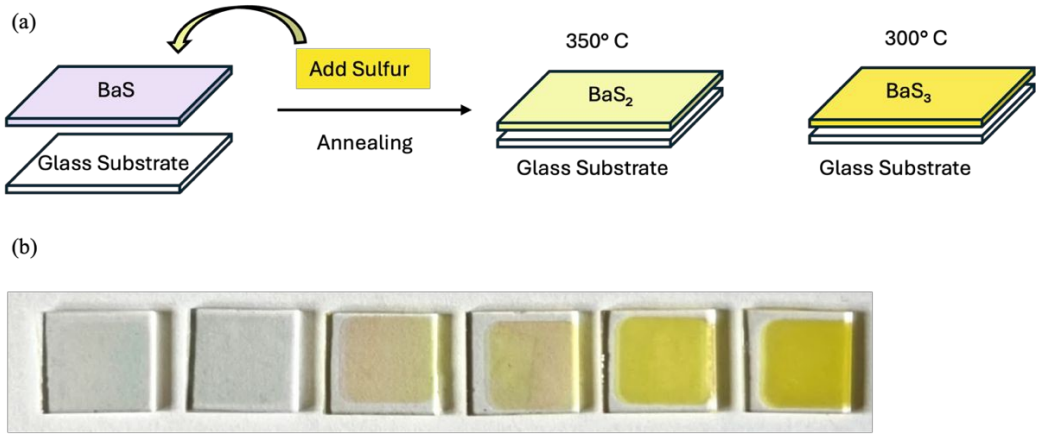

Figure (a) Schematic illustration showing the general approach of Fabrication of Ba-S films. (b)Visual representation of Ba-S samples. Samples 1–2: BaS, 3–4: BaS_2, 5–6: BaS_3

After annealing, the samples were cooled naturally inside the furnace under continuous nitrogen flow to prevent oxidation. Following sulfurization, noticeable color changes were observed: BaS_2 films developed a distinct red yellowish hue, confirming successful conversion, while BaS_3 films showed an even deeper yellow coloration shown in Figure 1(b).

Table 1 Experimental Parameters for the fabrication of thin films of Ba-S compounds

BaS				**Sulfurization**					**End Product**
Sample No	**Thickness (nm)**	**Rate (nm/s)**	**Amount of 'BaS' (mg)**	**Gas Flow (sccm)**	**Pressure (mbar)**	**Temperature (°C)**	**Annealing Time (min)**	**Amount of 'S' (mg)**	
1	350	0.2-0.3	80						BaS
2	350	0.2-0.3	80						BaS
3	300	0.1-0.2	80	100	30	350	30	85	BaS_2
4	300	0.1-0.2	80	100	30	350	30	85	BaS_2
5	250	0.1-0.2	80	50	10	300	30	80	BaS_3
6	350	0.2-0.3	80	50	10	300	30	80	BaS_3

Computational Details

First-principles density functional theory (DFT) calculations were performed using the Vienna *Ab initio* Simulation Package (VASP) [23–26]. The projector augmented-wave (PAW) method was employed to describe the electron–ion interactions. The initial crystal structures of BaS, BaS_2, and BaS_3 were obtained from the Materials Project database [27–30], as conventional thin-film X-ray diffraction cannot precisely resolve the internal fractional coordinates. Full structural relaxations, including lattice parameters, cell volume, and internal atomic positions (ISIF = 3), were carried out using the generalized gradient approximation (GGA) parameterized by Perdew, Burke, and Ernzerhof (PBE).

Convergence tests for the plane-wave cutoff energy and k-point mesh were rigorously conducted using the highly symmetric BaS phase. A k -point mesh density criterion of $a \times k \sim 20$ Å was established and consistently applied to generate the Monkhorst–Pack meshes for all structural phases. Although a cutoff energy of 500 eV was confirmed to be sufficient to ensure total-energy convergence and avoid Pulay stress during volume relaxation, a more stringent cutoff of 600 eV was conservatively applied for all calculations to guarantee high numerical precision. The electronic self-consistency criterion was tightly set to 1×10^{-8} eV.

View Article Online
DOI: 10.1039/D6MA00113K

Due to the significantly high computational cost, the Heyd–Scuseria–Ernzerhof (HSE06) hybrid functional was employed exclusively for the subsequent static electronic structure calculations on the PBE-optimized reference geometries. In the HSE06 calculations, the exact-exchange mixing parameter was fixed at 0.25, while the range-separation parameter (HFSCREEN, μ) was systematically varied from 0.0 to 0.4 $Å^{-1}$ to investigate its effect on the calculated band gaps and electronic screening [31,32].

Table 2 Optimized crystal structure (lattice parameter and atomic position)

Composition	Stoichiometry	Space group (No.)	a (Å)	b (Å)	c (Å)	α (°)	β (°)	γ (°)	a (Å) ICSD	b (Å) ICSD	c (Å) ICSD
Ba_4S_4	BaS	$Fm\bar{3}m$ (225)	6.4593	6.4593	6.4593	90	90	90	6.388	6.388	6.388
Ba_4S_8	BaS_2	C2/c (15)	9.3436	4.8386	9.1190	90	117.829	90	9.299	4.736	8.993
Ba_2S_6	BaS_3 (tetra.)	$P\bar{4}2_1m$ (113)	6.9843	6.9843	4.2360	90	90	90	6.881	6.881	4.177

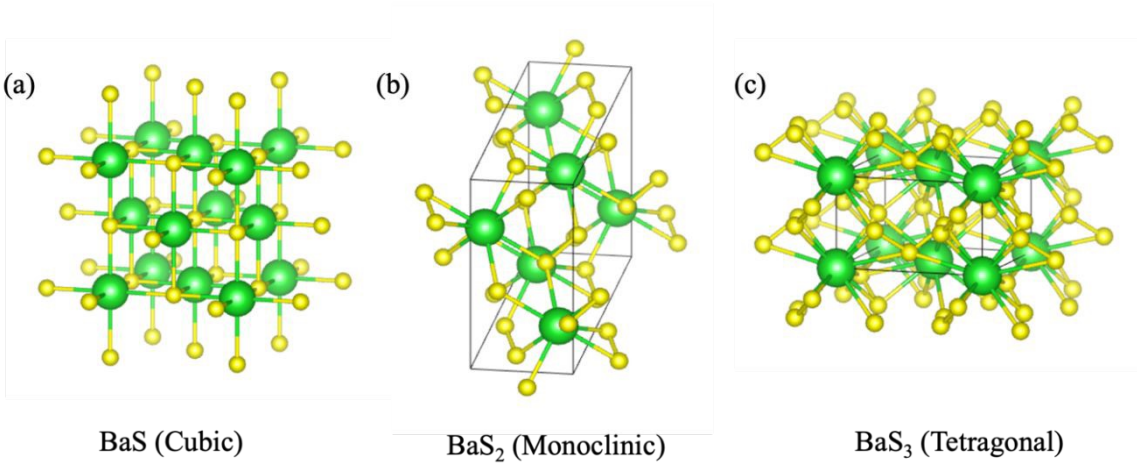

Figure 2 *Crystallographic Diagram of Ba-S compounds, (a) BaS cubic, (b) BaS_2 monoclinic, and (c) BaS_3 tetragonal. Large, green and small yellow spheres represent the Ba and S atoms, respectively.*

Characterization Technique

All six samples (**Table 1**) were characterized using four standard techniques: X-ray diffraction (XRD) for crystal structure identification, scanning electron microscopy (SEM) to observe surface morphology and grain size, energy-dispersive X-ray spectroscopy (EDS) to verify the Ba:S composition, and UV–Vis spectroscopy to determine the optical bandgap. Phase identification was performed using a PANalytical Empyrean diffractometer in Bragg–Brentano geometry with Cu Kα radiation (λ = 0.15406 nm). Data were collected in the range of 2θ = 10° to 50° with a 0.013° step size, and phase analysis was done using HighScore Plus software, with ICSD database support and Materials Project. The optical bandgap was determined at room temperature using UV-Vis spectroscopy. Transmittance data were analyzed using the Tauc plot

View Article Online
DOI: 10.1039/D6MA00113K

method to calculate the bandgap values. Absorbance spectra were acquired using a PerkinElmer Lambda 950 spectrometer with an integrating sphere and central mount holder. Samples were illuminated with a tungsten halogen lamp in the 200–800 nm range, and the transmitted radiation was detected by a R6872 photomultiplier. Microstructural examination and elemental composition analysis were conducted using scanning electron microscopy (SEM) combined with energy-dispersive X-ray spectroscopy (EDX). Samples were mounted on brass stubs with graphite tape, and images were obtained at an accelerating voltage of 15.0 kV using a JEOL JSM-7610 F system. EDX spectra were recorded at an accelerating voltage of 20 kV, using the X-Max 80 detector and AzTec Software from Oxford Instruments.

Results and Discussion

We successfully fabricated BaS, BaS_2 and BaS_3 thin films, which can be used to prepare BZS thin films when combined with elemental Zr. The crystal structures of the samples were determined using X-ray diffraction (XRD) measurements, and the phases were confirmed using HighScore software and Materials Project database and Inorganic Crystal Structure Database (ICSD) [20,21]. The X-ray diffractogram of the crystal product is presented in Figure 3. The XRD patterns showed good agreement with the reference patterns of the respective compounds and the additional curve observed in the XRD patterns for BaS_2 and BaS_3 corresponds to peaks from the glass substrate, which contribute to the background signal.

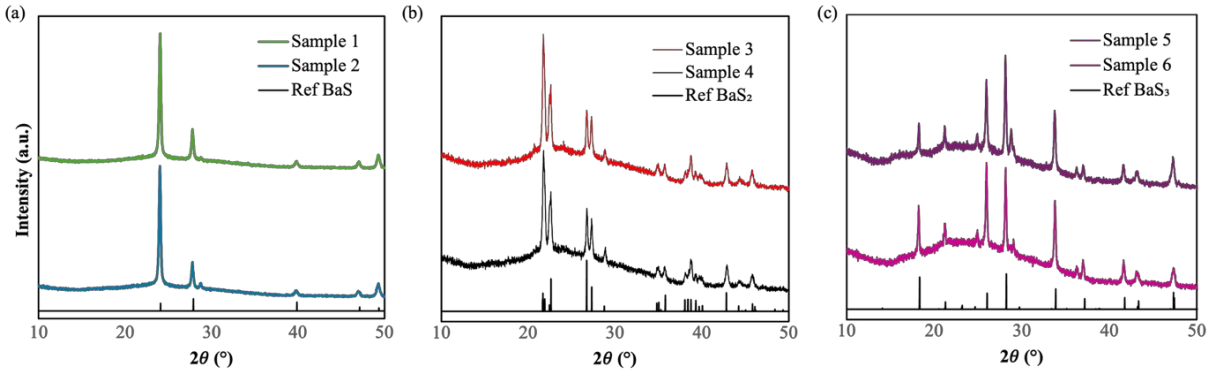

Figure 3 *X-ray diffraction (XRD) patterns of BaS (ICSD# 30240) (a), BaS_2 (ICSD# 2004) (b), and BaS_3 (CSD# 23637) (c) thin films. The patterns confirm single-phase formation for all films, as analyzed using High Score Plus.*

The XRD patterns of the deposited barium sulfide (BaS) samples 1 and 2 in Figure 3(a) show sharp peaks primarily between 20° and 50° 2θ, indicating a high degree of crystallinity [31,32,33]. Barium trisulfide (BaS_3) samples 5 and 6 also exhibit sharp and intense peaks, mainly between 20° and 40° 2θ, further reflecting their crystalline nature. In comparison, BaS_2 samples 3 and 4, which adopt a monoclinic structure, display less intense peaks, while BaS (cubic) and BaS_3 (tetragonal) show stronger diffraction peaks, consistent with their higher crystallinity.

We adopted crystal structures from prior studies and used them as references for phase identification. Due to the polycrystalline nature of the thin films, full structural refinement (atomic positions and lattice parameters) was not feasible from the experimental data alone. Therefore, well-established reference structures from the Materials Project were used. The agreement between experimental and reference diffraction patterns validates this approach. Crystalline regions were identified and compared against standard XRD patterns in Figure 3,

View Article Online
DOI: 10.1039/D6MA00113K

and the corresponding crystal structures for each phase are illustrated in Figure 2. For BaS_3, both tetragonal ($P\bar{4}2_1m$) and orthorhombic ($P2_12_12_1$) polymorphs are reported in the literature; According to Materials Project the tetragonal phase is thermodynamically stable and lies on the convex hull (E_{hull} = 0 eV/atom), whereas the orthorhombic variant is slightly metastable (E_{hull} ≈ 0.044 eV/atom) [29,30]. These results confirm that the experimentally observed phases correspond to thermodynamically stable configurations, while alternative polymorphs are slightly metastable. In our films, BaS (cubic, $Fm\bar{3}m$), BaS_2 (monoclinic, $C12/c1$), and BaS_3 (tetragonal, $P\bar{4}2_1m$) show excellent agreement between the experimental patterns and the reference data, consistent with E_{hull} = 0 eV/atom for these phases; the orthorhombic BaS_3 polymorph was not obtained under the present synthesis conditions.

The BaS_3 spectrum compared with the standard diffraction patterns, the observed peaks shown in Figure 3(c) correspond to characteristic planes such as (110), (200), and (211), confirming the formation of the expected phase without significant secondary phases. The agreement in relative intensities and the absence of extra peaks further verify the phase purity of the synthesized material [33]. HighScore Plus XRD analysis confirms that the synthesized BaS_3 adopts the tetragonal crystal structure. Consistent with literature, the structure features S_3^{2-} columns with Ba in a high (≈12-fold) S coordination, which rationalizes the observed intensity pattern[34].

The fabricated BaS_2 samples Figure 3(b) show distinct diffraction peaks that match the monoclinic phase [35,36]. The observed reflections can be indexed to the (101), (111), and (210) planes, confirming the formation of the expected phase without significant secondary phase contributions. The absence of additional peaks and the consistency of intensity ratios provide further evidence of phase purity. BaS_2 features arrays of S_2^{2-} disulfide units with Ba in an approximately eightfold S environment—motifs compatible with the observed pattern [37]. These results suggest that sulfur concentration is not the decisive factor controlling phase formation as multiple barium sulfide phases were obtained under the same sulfur level. Instead, temperature appears to play a more significant role in determining the final crystalline phase.

View Article Online
DOI: 10.1039/D0MA00113K

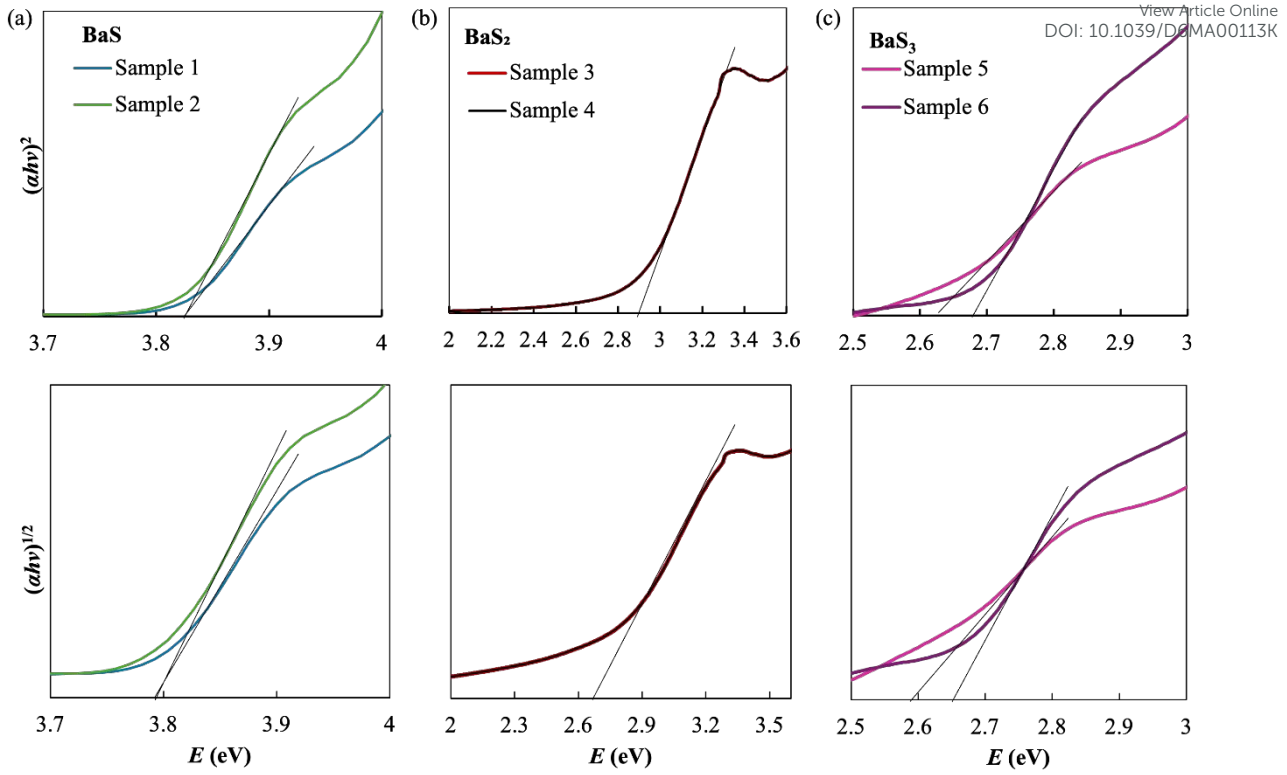

Figure 4 *Optical absorption data for BaS, BaS_2 and BaS_3 compounds represented as Tauc plots for both direct and indirect band gap transitions. The top row shows plots assuming direct allowed transitions (γ = 2), while the bottom row corresponds to indirect allowed transitions (γ = ½).*

Tauc plot analysis is a widely used method to estimate the optical band gap of semiconductors and thin film materials. The approach is based on the relation between the absorption coefficient (α) and the photon energy ($h\nu$), expressed as:

$$(\alpha h\nu)^{\gamma} = B\,(h\nu - E_g)$$

where E_g is the optical band gap, B is a proportionality constant, and γ is a factor that depends on the type of electronic transition. For direct allowed transitions, γ=2, while for indirect allowed transitions, γ=1/2. By plotting $(\alpha h\nu)^{\gamma}$ as a function of photon energy ($h\nu$), the band gap can be determined from the extrapolation of the linear region of the curve to the energy axis [38]. This method provides a reliable estimate of both direct and indirect band gaps and is particularly suitable for analyzing the optical properties of Ba–S thin films investigated in this work. It should be noted that the Tauc method provides an approximate description of the absorption edge and does not explicitly account for excitonic effects, defect states, or disorder. Therefore, the extracted band gaps should be interpreted as effective optical gaps rather than precise electronic band gaps.

The absorption coefficient (α) was calculated from transmittance using α = (1/d) ln(1/T), where d is the film thickness. A bare glass substrate was used as a reference to remove background contributions, and measurements were performed with an integrating sphere to minimize scattering effects. The uncertainty in the extracted band gap values was estimated by varying the linear fitting region of the Tauc plots, yielding an error of approximately ±0.05–0.1 eV.

As shown in Figure 4, both the direct and indirect bandgaps of the Ba–S compounds are presented. While we can estimate whether a material is likely to have a direct or indirect

View Article Online
DOI: 10.1039/D6MA00113K

bandgap, the band-gap nature cannot be determined conclusively from these measurements alone. Therefore, both values are reported for the barium sulfide compounds in this study.

BaS exhibits direct and indirect absorption onsets at approximately 3.82 eV and 3.78 eV, respectively, consistent with experimental and theoretical reports that identify BaS as an indirect-gap semiconductor [39]. BaS and related chalcogenides have been modeled in prior computational research employing FP-LAPW methodologies (e.g., EV-GGA), which support a broader indirect bandgap in comparison to lattice scaling behavior. While some thin-film optical measurements suggest lower apparent bandgaps (~1.3 eV) due to defect states or non-stoichiometry, our data align closely with the intrinsic bulk-phase values [40].

For BaS_2, first-principles calculations imply that its lower dimensionality and altered electronic structure result in a narrower bandgap compared to BaS. These calculations predict direct and indirect absorption onsets at approximately 2.9 eV and 2.69 eV, respectively, aligning with trends towards extended absorption into the visible spectrum as observed in our measurements. BaS_3 exhibits direct and indirect optical onsets at approximately 2.65-2.69 and 2.58-2.65 eV, respectively. Additionally, BaS_3 appears to show a second absorption event at higher energies possibly due to a separate energy transition requiring energies slightly higher than the main energies transition. An absorption feature at ~3.28 eV is attributed to intrinsic point defects, which may act as shallow donors or acceptors above the bandgap. To further validate the bandgap, we analyzed the absorption coefficient of the films, which indicates an indirect bandgap around 470 nm, comparable to silicon absorption coefficient data shown in Figure S2. While direct optical measurements of BaS_3 thin films have been reported, computational studies of related chalcogenides, such as $BaZrS_3$ (calculated bandgap ~1.8 eV), suggest that a redshift in BaS_3 absorption edge is plausible due to its bonding and structural motifs. Our experimental results are consistent with this anticipation.

The experimentally observed reduction in band gap from BaS to BaS_2 and BaS_3 is consistent with the structural evolution toward increased sulfur coordination and S–S bonding. This trend is further supported by the DFT results, which show increased S 3p contributions near the valence-band edge and a corresponding narrowing of the band gap. This agreement between experiment and theory highlights the strong coupling between crystal structure and electronic properties in Ba–S compounds.

Consistent with the structural evolution summarized in Table 2 and illustrated in Table 3,
increasing sulfur content drives a transition from simpler cubic structures to more complex monoclinic and tetragonal systems and is accompanied by shorter S–S bond lengths (≈2.118 Å in BaS_2 [34] and ≈2.074 Å in BaS_3 [37]). These shorter bonds can potentially lead to stronger S-S interactions. These structural changes influence the local environment of the barium ions, affecting the overall electronic structure of the material. Consequently, the increased bonding strength between sulfur atoms and a more ordered arrangement could reduce the electronic states near the Fermi level, potentially leading to a narrower bandgap, which would be significant for optimizing the compound's performance in optoelectronic applications, such as photovoltaics.

Table 3 Structural parameters for BaS_2 and BaS_3, anionic units, intramolecular S–S distances, closest inter-anion S···S contacts, Ba–S distances (X= Chalcogen atom)

Compound	Structure type / SG (No.)	Anionic unit	X–X (intramolecular) (Å)	Closest inter-anion X···X (Å)	Ba–X distances (Å)	Ba coordination	Reference
BaS_2	Monoclinic C2/c (15)	$(S_2)^{2-}$ dimers	**2.118**	3.143 (shortest), 3.21–3.98	3.151–3.223	8	Yamako et al. [41]
BaS_3	Tetragonal $P4_2im$ (113)	$(S_3)^{2-}$ trimers	**2.074**	3.388(7)	3.204(7), 3.344(7), 3.541(1)	12	Kawada et al. [35]

SEM and EDX analyses were performed to assess the morphology and elemental composition of the BaS, BaS_2, and BaS_3 thin films. Figures 5a, b, and c illustrate the topographical features of the films at both low and high magnifications. The BaS_2 and BaS_3 films are predominantly polycrystalline, with their morphology evolving in response to increasing sulfur content. Specifically, the sulfur-rich films (BaS_2 and BaS_3) exhibit a significant increase in porosity, displaying abundant pores and voids, accompanied by unevenly faceted grains. In contrast, the near-stoichiometric BaS films are characterized by a compact, homogeneous microstructure, composed of uniformly sized nanograins (~20–30 nm), indicative of lower sulfur content and controlled crystallization.

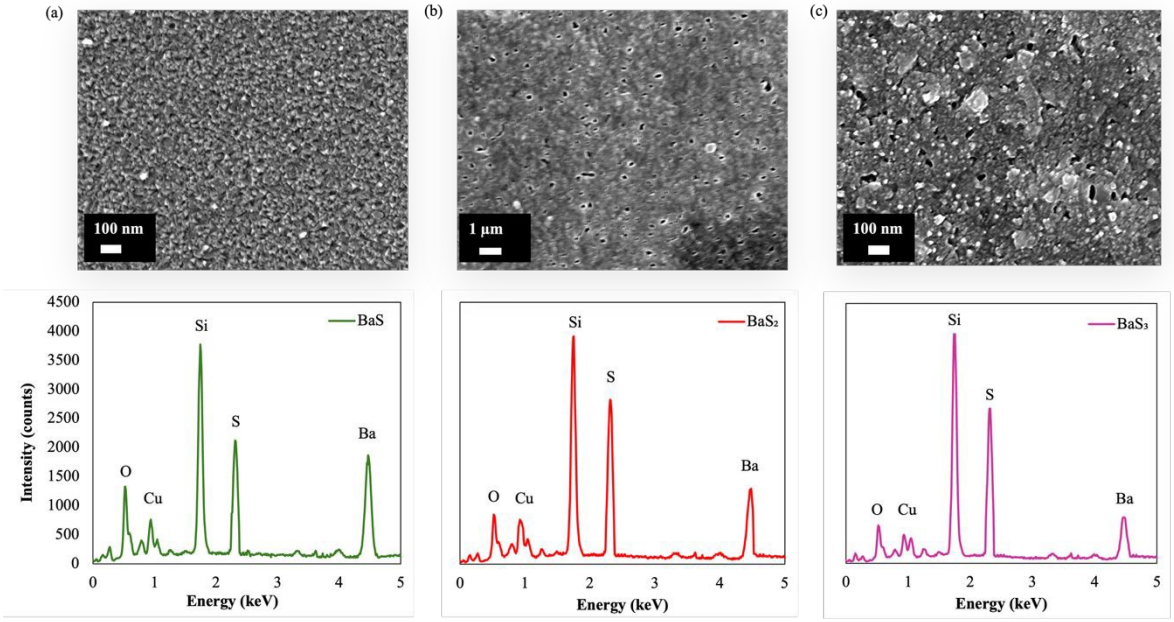

Figure 5. *SEM (top) and EDX (bottom) images of Ba–S thin films after sulfurization: (a) BaS exhibits a dense, nanocrystalline microstructure with minimal porosity and an approximately 1:1 Ba:S EDX peak ratio; (b) BaS_2 shows a porous surface with sub-100 nm pits and an approximately 1:2 Ba:S EDX peak ratio; and (c) BaS_3 displays a rough, faceted microstructure with numerous elongated voids and an approximately 1:3 Ba:S EDX peak ratio.*

EDX spot analyses confirmed the expected stoichiometries for each film: ~51/49 (S/Ba) for BaS, ~66/34 (S/Ba) for BaS_2, and ~74/26 (S/Ba) for BaS_3 shown in Figure 5 and Table 4 confirming precise control over the sulfurization process. The corresponding EDX spectra of Ba-S films showed clear peak ratios for Ba and S, validating the accuracy of the sulfur content

View Article Online
DOI: 10.1039/D6MA00113K

in each film. Additionally, peaks for Si and O are attributed to the glass substrate, as the films are extremely thin and the electron beam penetrates beyond 1 micron. The Cu peak is associated with the conductive tape and holder, used to improve conductivity, as the substrate is insulating. The reported compositions represent averages over multiple (>5) measurement points, with a variation of less than ±2 at%. Minor oxygen signals originate from the glass substrate and were excluded from the compositional analysis.

Table 4 EDX Data of Ba-S composition ratio of samples of 1-6

Sample	S (at%)	Ba (at%)
BaS	51.2	48.8
BaS_2	66.1	33.9
BaS_3	73.8	26.2

The observed increase in porosity in the sulfur-rich BaS_2 and BaS_3 films aligns with the high sulfur chemical potential during the sulfurization process. This high sulfur content promotes Kirkendall voiding and sulfur out-diffusion, phenomena commonly observed in sulfur-rich systems. In contrast, the stoichiometric BaS films exhibit a dense and continuous microstructure, with minimal porosity, reflecting the lower sulfur content [40,42]. These findings are consistent with the XRD phase assignments, which further highlight the structural differences between the films driven by varying sulfur concentrations.

DFT Calculations

The electronic density of states (DOS) for BaS, BaS_2, and two BaS_3 polymorphs—tetragonal and orthorhombic—was computed using the semilocal Perdew–Burke–Ernzerhof (PBE) functional and HSE-type screened hybrid functionals [43,44]. In all hybrid-functional calculations, the exact-exchange mixing parameter was fixed at $\alpha = 0.25$, while the range-separation parameter HFSCREEN (μ) was systematically varied. In this framework, α controls the overall strength of the Hartree–Fock (HF) exchange, whereas μ determines its spatial range—i.e., the degree of electronic screening. Thus, only the range of the HF exchange is modified, allowing the effect of local screening to be examined independently of exchange strength. As expected, PBE systematically underestimates the electronic band gap, whereas the screened hybrids provide improved accuracy through the inclusion of short-range Hartree–Fock (HF) exchange. To directly compare the experimental optical band gaps with the theoretical predictions, Figure 7 and Table 7 summarize the band gaps of all Ba–S compounds obtained from both measurements and first-principles calculations. The experimental direct and indirect band gaps extracted from the Tauc plots are presented alongside the calculated values obtained using the PBE functional and the HSE06 hybrid functional with different HFSCREEN (μ) parameters. As shown in Figure 7, PBE systematically underestimates the gaps for all phases, particularly for the sulfur-rich BaS_2 and BaS_3 compounds. In contrast, the HSE06 calculations—with μ values chosen consistently with structural symmetry and local bonding—reproduce the experimental band gaps with high accuracy. These results establish the basis for the following discussion of the electronic structure and screening effects across the Ba–S series.

View Article Online
DOI: 10.1039/D6MA00113K

In this work, the μ parameter varied systematically and selected to reproduce the experimental band gaps while remaining consistent with expected trends in electronic screening. Although μ is not determined from first principles in this approach, its variation provides insight into how local bonding and structural symmetry influence effective electronic screening in Ba–S compounds [45]. The trend μ = 0.00 Å^{-1} for cubic BaS, μ ≈ 0.15 Å^{-1} for tetragonal BaS_3, and μ ≈ 0.25 Å^{-1} for monoclinic BaS_2 reflects the progressive symmetry lowering and increasing S–S coordination, which enhance electronic polarization and thus the effective screening of the exchange interaction. This means that the strength of the HF exchange is constant, and only its spatial range (i.e., the degree of electronic screening) is being systematically examined.

To further establish this link, μ was varied over a range of 0.0–0.4 Å^{-1}. A sensitivity analysis shows that varying μ by ±0.05 Å^{-1} changes the band gap by approximately 0.1–0.2 eV, indicating that the conclusions are robust against small variations in this parameter (≤ 0.3 eV across all phases). This confirms that our conclusions do not rely on fine tuning and that μ can be interpreted as a physically motivated measure of local electronic screening. Lower symmetry and stronger S–S coordination in BaS_3 and BaS_2 are consistent with larger μ values, whereas highly symmetric and more ionic BaS phase require little or no screening (μ ≈ 0). These results directly connect crystal structure, electronic screening, and hybrid-functional band gaps across the Ba–S series.

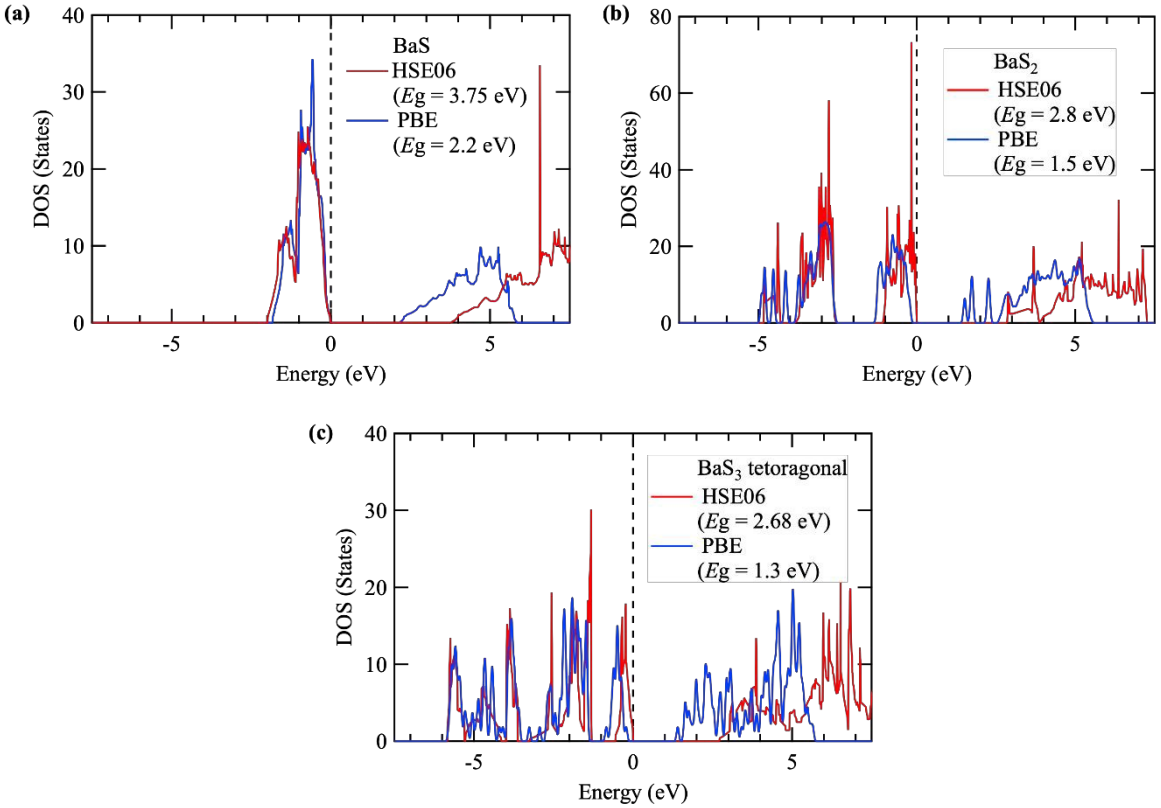

Figure 6. Total electronic density of states (DOS) for (a) BaS, (b) BaS_2, and (c) tetragonal BaS_3 calculated using the PBE (blue) and HSE06 (red) functionals. Energies are referenced to the valence-band maximum (VBM = 0 eV, dashed line). Band gaps estimated from the DOS are BaS = 3.75 eV (HSE06), 2.2 eV (PBE); BaS_2 = 2.8 eV (HSE06), 1.5 eV (PBE); and BaS_3 (tetragonal) = 2.68 eV (HSE06), 1.3 eV (PBE). The trend BaS > BaS_2 > BaS_3 reflects increasing sulfur coordination and S–S bonding, which introduce additional states near the

View Article Online
DOI: 10.1039/D6MA00113K

band edges and narrow E_g. The HSE06 hybrid functional (HFSCREEN from 0.00 Å^{-1} for BaS to 0.25 Å^{-1} for BaS_2 and 0.15 Å^{-1} for BaS_3) consistently predicts wider gaps than PBE.

As shown in Figure 6 and Figure S3, the HSE06 band gaps consistently exceed the PBE values across all phases, with the orthorhombic BaS_3 showing the smallest gap of 2.21 eV (HSE06). The systematic reduction of *Eg* from BaS to BaS_2 and BaS_3 reflects the increasing sulfur content and the presence of S–S bonding units, which introduce additional states close to the valence-band maximum, suggests that as symmetry decreases, local distortions and S–S bonding enhance electronic polarization, leading to stronger screening and thus a larger μ (shorter-range exchange). The valence-band edge is dominated by S 3p orbitals, whereas the conduction band primarily originates from Ba 5d states with minor 6s contributions. The progressive hybridization of S–S and S–Ba orbitals increase the DOS near the edges, leading to the observed narrowing of Eg as sulfur coordination becomes more extended.

We note that spin-orbital coupling (SOC) is generally important for compounds containing heavy elements. In the present Ba–S systems, however, the band edges are mainly derived from S 3p and Ba occupied 6s and unoccupied 5d states, for which SOC effects are expected to be small (~0.05–0.15 eV at the edges). Moreover, the hybrid-functional results without SOC already reproduce the experimental band gaps very well. Including SOC would roughly double the computational cost, and although it might shift the band gap by ~0.1 eV, such a change is within the uncertainty of the present HSE parameter setup and does not affect the conclusions of this work.

Overall, the HSE06 results demonstrate that Ba–S binary and polysulfide compounds are wide-gap semiconductors, transparent in the visible and absorbing primarily in the near-UV. In contrast, PBE would incorrectly predict near-IR or visible absorption for BaS_2 and BaS_3. Thus, hybrid-functional approaches are essential for reliable predictions of electronic properties in Ba–S systems. The comparison between the two BaS_3 polymorphs also highlights a structure–property relationship: the orthorhombic phase exhibits stronger local distortions and enhanced orbital overlap, lowering the conduction-band minimum and resulting in a smaller E_g compared to the tetragonal form.

For BaS_3, both tetragonal ($P\bar{4}2_1m$) and orthorhombic ($P2_12_12_1$) polymorphs are reported in the literature. To theoretically validate our experimental phase assignments and understand the thermodynamic driving forces, we calculated the formation energies (ΔH_f) of these phases using fully relaxed PBE total energies (summarized in Table 5). The calculated formation energies for BaS, BaS_2, and tetragonal BaS_3 are highly negative: -4.156 eV/f.u., -4.257 eV/f.u., and -4.237 eV/f.u., respectively. These results highlight the strong thermodynamic stability of these compounds and their viability as stable intermediate phases. Furthermore, our calculations reveal that the tetragonal BaS_3 phase is energetically more favorable than the orthorhombic BaS_3 phase (-4.132 eV/f.u.) by approximately 0.1 eV/f.u. This theoretical finding perfectly supports both the Materials Project energetics [46] and our experimental observation where only the tetragonal phase was obtained under the present synthesis conditions.
In our films, BaS (cubic, $Fm\bar{3}m$), BaS_2 (monoclinic, $C12/c1$), and BaS_3 (tetragonal, $P\bar{4}2_1m$) show excellent agreement between the experimental patterns and the reference data, consistent with E_{hull} = 0 eV/atom for these phases; the orthorhombic BaS_3 polymorph was not obtained under the present synthesis conditions.

Table 5. Calculated PBE total energies and formation energies (ΔH_f) of Ba-S phases.

View Article Online
DOI: 10.1039/D6MA00113K

Stoichiometry	Space group (No.)	E_{tot} per f.u. (eV)	ΔH_f (eV/f.u.)
BaS	$Fm\bar{3}m$ (225)	-10.216	-4.156
BaS_2	C2/c (15)	-14.447	-4.257
BaS_3 (tetra.)	$P\bar{4}2_1m$ (113)	-18.560	-4.237
BaS_3 (ortho.)	$P2_12_12_1$ (18)	-18.455	-4.132

The reason why the order of μ does not simply correlate with the macroscopic dielectric constant is that this system is governed by two independent physical factors: 'microscopic structural symmetry breaking' and 'macroscopic polysulfide chain topology.' The range-separation parameter μ (microscopic exchange screening) directly couples with the enhancement of local field effects induced by the reduction of space group symmetry. Conversely, the maximum static dielectric constant ε∞ observed in BaS3 arises from the large dynamic polarization associated with the elongation of the S3(2-) trimer chain, as evidenced by the severe splitting of the Born effective charges (+0.08 / -1.55). Therefore, our choice of parameters is fully justified by clear crystal-chemical necessities rather than arbitrary fitting.

To further support this interpretation, Table 6 presents the static dielectric constants (ε∞) and Born effective charges (Z*) calculated using PBE for all three phases [47,48]. The static dielectric constant increases progressively from BaS (ε∞ = 4.806) to BaS_2 (4.965) and BaS_3 (5.906), reflecting the enhanced electronic polarizability associated with increasing sulfur coordination and S–S bond formation. The Born effective charges show a clear evolution across the series: in BaS, the charges are symmetric (Ba: +2.61, S: −2.61), consistent with the highly ionic cubic structure. In BaS_2, the S charge reduces to −1.33, reflecting partial covalent character introduced by the S_2^{2-} dimer units. In BaS_3, a striking asymmetry appears between the two inequivalent sulfur sites (+0.08 and −1.55), which arises from the dynamical polarization of the elongated S_3^{2-} trimer chain. This large charge splitting is the microscopic origin of the elevated ε∞ in BaS_3 and directly explains why a larger μ value is not required for this phase despite its lower symmetry — the macroscopic screening is already enhanced through chain polarization rather than local exchange effects.

Table 6. Static dielectric constants (ε∞) and Born effective charges (Z) calculated using PBE for BaS, BaS_2, and BaS_3, illustrating the progressive enhancement of electronic polarizability across the Ba–S series.*

Phase	**ε∞**	**Born Effective Charges** (Z*)
BaS	4.806	Ba: +2.61, S: −2.61
BaS_2	4.965	Ba: +2.65, S: −1.33

View Article Online
DOI: 10.1039/D6MA00113K

BaS_3	5.906	Ba: +3.02, S: −1.55 / +0.08

Table 7. Overall Bandgaps of Ba–S compounds obtained from experimental measurements and theoretical calculations.

Phase	μ = 0.00 Å⁻¹	μ = 0.10 Å⁻¹	μ = 0.15 Å⁻¹	μ = 0.20 Å⁻¹ (default)	μ = 0.25 Å⁻¹	Experiment Direct gap (eV)	Experiment Indirect gap (eV)
BaS	3.8	—	—	3.1	—	3.8	3.8
BaS_2	—	—	—	2.8	2.7	2.9	2.7
BaS_3 (tetra.)	—	—	2.7	2.5	—	2.7	2.6

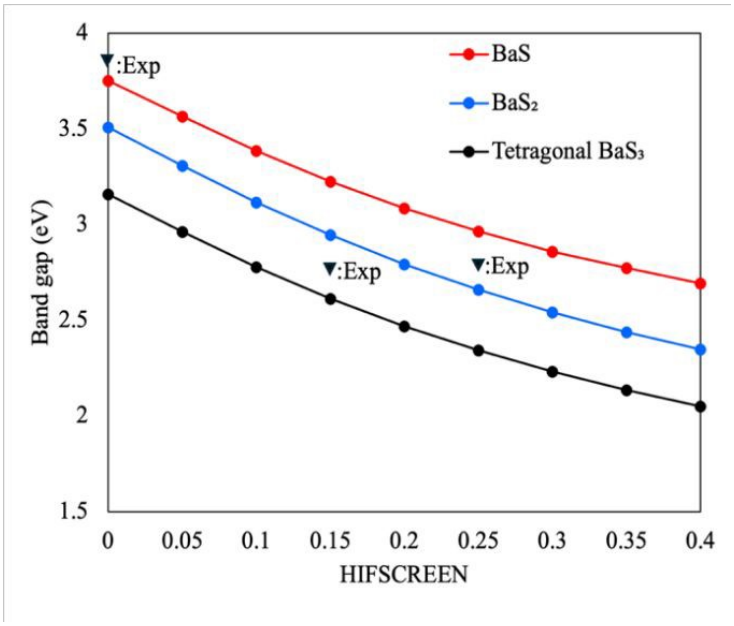

Figure 7. Comparison of HSE06 calculated and experimental band gaps for BaS, BaS_2, and BaS_3 as a function of HFSCREEN (μ) parameter.

Importantly, these results highlight the role of the HFSCREEN parameter in HSE06. As shown by Krukau et al. [44], decreasing HFSCREEN (extending the range of exact exchange) increases the computed band gap, whereas increasing HFSCREEN (stronger screening) reduces it. This tuning is particularly relevant for BaS_3, where sulfur-chain motifs and local distortions enhance the sensitivity to nonlocal exchange. A conceptual parallel exists with 1T-TaS_2, where stacking periodicity governs quasi-1D band dispersion in the commensurate CDW [44] ; likewise, adjusting HFSCREEN modulates the effective exchange range and the localization/delocalization balance in Ba–S polysulfides. More broadly, hybrid-functional indicate that incorporating screened exact exchange provides more reliable band-gap predictions than semilocal DFT, particularly for materials in which local bonding motifs and electronic screening vary strongly across structural polymorphs. In this context, μ provides a useful phenomenological descriptor of effective electronic screening in Ba–S compounds [45].

View Article Online
DOI: 10.1039/D6MA00113K

Conclusion

In this work, we successfully synthesized BaS, BaS_2, and BaS_3 thin films through electron-beam evaporation followed by controlled sulfurization. XRD analysis verified the formation of cubic BaS, monoclinic BaS_2, and tetragonal BaS_3, demonstrating that precise phase control is achievable solely through temperature- and sulfur-mediated pathways. The corresponding optical measurements revealed a clear and reproducible reduction in the band gap across the series, confirming the strong influence of sulfur coordination and crystal symmetry on the electronic structure. Hybrid-functional calculations using HSE06 with a fixed mixing parameter ($\alpha = 0.25$) and a variable HFSCREEN (μ) reproduced the experimental band gaps with high accuracy. The optimized μ values follow the symmetry sequence BaS ($\mu = 0.00$) < BaS_3 ($\mu \approx 0.15$) < BaS_2 ($\mu \approx 0.25$), demonstrating that lower symmetry and stronger S–S bonding enhance local electronic screening. Overall, this study establishes a clear relationship between crystal symmetry, sulfur coordination, electronic screening, and band-gap formation in Ba–S compounds. The HFSCREEN-tuned hybrid-functional approach provides a reliable pathway for predicting and engineering the electronic properties of sulfide-based materials for optoelectronic applications.

Acknowledgements

This study was supported by the Deutsche Forschungsgemeinschaft (Grant No. GRK2495/2/I), the Japan Society for the Promotion of Science (JSPS) Japanese-German Graduate Externship (Grant No. 2019/R1), and JSPS Scientific Research (A) (Grant No. 25H00606). The author is grateful to Mr. Mingjie Feng (Department of Materials Science and Engineering 6, Friedrich-Alexander-University Erlangen-Nürnberg) and Mr. Kongshik Rho (Electrical and Mechanical Engineering, Nagoya Institute of Technology) for helpful discussions.

Author contributions

K.H., H.M., and P.W. conceived the idea. S.J. designed the research, fabricated the thin films, performed the XRD, SEM, EDX, and UV–Vis analyses, analyzed the data, prepared the illustrations, and wrote the first draft of the manuscript. K.H. and P.W. supervised the research. H.M. contributed to the DFT calculations. H.M., K.H., K.K., and P.W. revised the manuscript. All the authors revised and approved the manuscript.

Data Availability

All data supporting the findings of this study are openly available within the article and its Electronic Supplementary Information (ESI), including X-ray diffraction patterns, UV–Vis absorption spectra, SEM and EDX data, crystallographic parameters, and DFT results. Optimized crystal structures and raw computational files are available from the corresponding author upon reasonable request.

Funding

The authors would like to express their sincere gratitude for the financial support by the Deutsche Forschungsgemeinschaft (Grant No. GRK2495/2/I), the Japan Society for the Promotion of Science (JSPS) Japanese-German Graduate Externship (Grant No. 2019/R1), and JSPS Scientific Research (A) (Grant No. 25H00606).

Competing interests

The authors declare no competing interests.

View Article Online
DOI: 10.1039/D6MA00113K

References:

1 K. Ye, I. Sadeghi, M. Xu, J. Van Sambeek, T. Cai, J. Dong, R. Kothari, J. M. LeBeau and R. Jaramillo, *Adv. Funct. Mater.*, 2024, **34**, 2405135.
2 T. Freund, M. R. Cicconi and P. J. Wellmann, *Phys. Status Solidi B*, 2022, **259**, 2200094.
3 M. Feng, J. Byun, Z. Li, Z. Xie, W. Lu, X. Wen, L. Ding, T. Wu, S. Jamshaid, K. Götz, C. Li, Z. Peng, H. Hu, J. Tian, J. Elia, T. Unruh, M. Halik, D.-J. Xue, A. Osvet and C. J. Brabec, *Nat. Commun.*, 2025, **16**, 9891.
4 S. Jamshaid, M. R. Cicconi, W. Heiss, K. G. Webber and P. J. Wellmann, *Adv. Eng. Mater.*, 2024, **26**, 2302161.
5 J. W. Turnley and R. Agrawal, *Chem. Commun.*, 2024, **60**, 5245–5269.
6 I. Sadeghi, K. Ye, M. Xu, Y. Li, J. M. LeBeau and R. Jaramillo, *Adv. Funct. Mater.*, 2021, **31**, 2105563.
7 D. C. Hayes, O. Z. Choudhry, S. Agarwal, K. C. Vincent, H. Belmonte and R. Agrawal, *Nanoscale Adv.*, 2025, **7**, 7653–7662.
8 R. Nielsen, in *Ullmann's Encyclopedia of Industrial Chemistry*, ed. Wiley-VCH Verlag GmbH & Co. KGaA, Wiley-VCH Verlag GmbH & Co. KGaA, Weinheim, Germany, 2000, p. a28_543.
9 R. Woods-Robinson, Y. Han, H. Zhang, T. Ablekim, I. Khan, K. A. Persson and A. Zakutayev, *Chem. Rev.*, 2020, **120**, 4007–4055.
10 T. B. Massalski, *Metall. Trans. A*, 1989, **20**, 1295–1323.
11 J. Ramanujam and U. P. Singh, *Energy Environ. Sci.*, 2017, **10**, 1306–1319.
12 T. Freund, S. Jamshaid, M. Monavvar and P. Wellmann, *Crystals*, 2024, **14**, 267.
13 Ł. Szeleszczuk, K. Mądra-Gackowska and M. Gackowski, *J. Phys. Chem. Solids*, 2026, **213**, 113575.
14 Ł. Szeleszczuk, K. Mądra-Gackowska, K. Szewczyk-Golec and M. Gackowski, *Comput. Condens. Matter*, 2025, **45**, e01153.
15 F. Hulliger and T. Siegrist, *Z. Für Naturforschung B*, 1981, **36**, 14–15.
16 M. G. Kanatzidis, *Chem. Mater.*, 1990, **2**, 353–363.
17 G. Li, S. Wang, Y. Zhang, M. Li, Z. Chen and J. Lu, *Adv. Mater.*, 2018, **30**, 1705590.
18 Á. Morales-García, R. Valero and F. Illas, *J. Phys. Chem. C*, 2017, **121**, 18862–18866.
19 A. J. Cohen, P. Mori-Sánchez and W. Yang, *Science*, 2008, **321**, 792–794.
20 I. Jihad, M. H. S. Anfa, S. M. Alqahtani and F. H. Alharbi, *Comput. Mater. Sci.*, 2024, **244**, 113153.
21 A. J. Garza and G. E. Scuseria, *J. Phys. Chem. Lett.*, 2016, **7**, 4165–4170.
22 A. Förster and F. Bruneval, *J. Phys. Chem. Lett.*, 2024, **15**, 12526–12534.
23 G. Kresse and J. Furthmüller, *Comput. Mater. Sci.*, 1996, **6**, 15–50.
24 G. Kresse and J. Furthmüller, *Phys. Rev. B*, 1996, **54**, 11169–11186.
25 G. Kresse and J. Hafner, *Phys. Rev. B*, 1993, **47**, 558–561.
26 G. Kresse and D. Joubert, *Phys. Rev. B*, 1999, **59**, 1758–1775.
27 Materials Data on BaS by Materials Project, 2020.
28 Materials Data on BaS_2 by Materials Project, 2020.
29 Materials Data on BaS_3 by Materials Project, 2020.
30 Materials Data on BaS_3 by Materials Project, 2020.
31 J. Heyd, G. E. Scuseria and M. Ernzerhof, *J. Chem. Phys.*, 2003, **118**, 8207–8215.
32 A. Jain, S. P. Ong, G. Hautier, W. Chen, W. D. Richards, S. Dacek, S. Cholia, D. Gunter, D. Skinner, G. Ceder and K. A. Persson, *APL Mater.*, 2013, **1**, 011002.
33 T. M. Henderson, B. G. Janesko and G. E. Scuseria, *J. Chem. Phys.*, 2008, **128**, 194105.
34 I. Kawada, K. Kato and S. Yamaoka, *Acta Crystallogr. B*, 1975, **31**, 2905–2906.
35 P. R. Jubu, E. Danladi, U. I. Ndeze, O. Adedokun, S. Landi, A. J. Haider, A. T. Adepoju, Y. Yusof, O. S. Obaseki and F. K. Yam, *Results Opt.*, 2024, **14**, 100606.
36 T. Lv, D. Chen and M. Huang, *J. Appl. Phys.*, 2006, **100**, 086103.

37 Y. Chen, S. W. Fan and G. Y. Gao, *Phys. Chem. Chem. Phys.*, 2023, **25**, 11745–11755.
38 G. Kalpana, B. Palanivel and M. Rajagopalan, *Phys. Rev. B*, 1994, **50**, 12318–12325.
39 M. Kim, H. Seok, N. Clament Sagaya Selvam, J. Cho, G. H. Choi, M. G. Nam, S. Kang, T. Kim and P. J. Yoo, *J. Power Sources*, 2021, **493**, 229688.
40 S. Yamaoka, J. T. Lemley, J. M. Jenks and H. Steinfink, *Inorg. Chem.*, 1975, **14**, 129–131.
41 Y. Wang, Y. R. Bian and M. X. Huang, *Acta Mater.*, 2025, **289**, 120938.
42 J. E. Moussa, P. A. Schultz and J. R. Chelikowsky, *J. Chem. Phys.*, 2012, **136**, 204117.
43 A. V. Krukau, O. A. Vydrov, A. F. Izmaylov and G. E. Scuseria, *J. Chem. Phys.*, 2006, **125**, 224106.
44 P. Borlido, J. Schmidt, A. W. Huran, F. Tran, M. A. L. Marques and S. Botti, *Npj Comput. Mater.*, 2020, **6**, 96.
45 D. Zagorac, K. Doll, J. Zagorac, D. Jordanov and B. Matović, *Inorg. Chem.*, 2017, **56**, 10644–10654.
46 X. Gonze and C. Lee, *Phys. Rev. B*, 1997, **55**, 10355–10368.
47 S. Baroni, S. De Gironcoli, A. Dal Corso and P. Giannozzi, *Rev. Mod. Phys.*, 2001, **73**, 515–562.

View Article Online
DOI: 10.1039/D6MA00113K

Data Availability

All data supporting the findings of this study are openly available within the article and its Electronic Supplementary Information (ESI), including X-ray diffraction patterns, UV–Vis absorption spectra, SEM and EDX data, crystallographic parameters, and DFT results. Optimized crystal structures and raw computational files are available from the corresponding author upon reasonable request.